

Computational study of non-Newtonian Eyring–Powell fluid from a vertical porous plate with biot number effects

S. Abdul Gaffar¹ · V. Ramachandra Prasad² · Bhuvana Vijaya³

Received: 26 February 2015 / Accepted: 13 March 2017 / Published online: 22 March 2017
© The Brazilian Society of Mechanical Sciences and Engineering 2017

Abstract In this article, the nonlinear, steady-state boundary layer flow and heat transfer of an incompressible Eyring–Powell non-Newtonian fluid from a vertical porous plate is investigated. The transformed conservation equations are solved numerically subject to physically appropriate boundary conditions using a second-order versatile, implicit finite-difference Keller Box technique. The numerical code is validated with previous studies. The influence of a number of emerging non-dimensional parameters, namely Eyring–Powell rheological fluid parameters (ε), the local non-Newtonian parameter based on length scale x (δ), Prandtl number (Pr), Biot number (γ) and dimensionless tangential coordinate (ξ) on velocity and temperature evolution in the boundary layer regime are examined in detail. Furthermore, the effects of these parameters on *surface heat transfer rate* and *local skin friction* are also investigated. It is found that the velocity is reduced with increasing ε but temperature is increased. Increasing δ enhances velocity but reduces temperature. The increasing γ is observed to enhance both velocity and temperature. And an increasing Prandtl number Pr is found to decrease both velocity and temperature.

Keywords Non-Newtonian fluid · Eyring–Powell model · Vertical plate · Finite difference numerical method · Heat transfer · Boundary layers · Skin friction · Nusselt number · Biot number · Fluid parameters

Abbreviations

Nomenclature

| | |
|--------|--|
| C | Fluid parameter, (time) ⁻¹ |
| C_f | Skin friction coefficient |
| f | Non-dimensional steam function |
| g | Acceleration due to gravity, m/s ² |
| Gr_x | Grashof (free convection) number |
| k | Thermal conductivity, kg m s ⁻³ K ⁻¹ |
| K | Thermal diffusivity, m ² /s |
| Nu | Local Nusselt number |
| Pr | Prandtl number |
| T | Temperature of the fluid, K |
| u, v | Non-dimensional velocity components along the x - and y - directions, respectively |
| V | Velocity vector, m/s |
| x | Stream wise coordinate |
| y | Transverse coordinate |

Greek symbols

| | |
|---------------|---|
| α | Thermal diffusivity, m ² /s |
| ε | Fluid parameter |
| β | Fluid parameter |
| β_I | Coefficient of thermal expansion, ppm/ °F |
| δ | The local non-Newtonian parameter based on length scale x |
| γ | Biot number |
| η | Dimensionless radial coordinate |
| μ | Dynamic viscosity, Ns/m ² |
| ν | Kinematic viscosity, Ns/m ² |

Technical Editor: Cezar Negrao.

✉ S. Abdul Gaffar
abdulsgaffar0905@gmail.com

¹ Department of Mathematics, Salalah College of Technology, Salalah, Oman

² Department of Mathematics, Madanapalle Institute of Technology and Science, Madanapalle 517325, India

³ Department of Mathematics, Jawaharlal Nehru Technology University Anantapur, Anantapuramu, India

| | |
|----------|---|
| θ | Non-dimensional temperature |
| ρ | Density of the fluid, kg/m ³ |
| ξ | Dimensionless tangential coordinate |
| ψ | Dimensionless stream function |

Subscripts

| | |
|----------|------------------------------------|
| w | Surface conditions on plate (wall) |
| ∞ | Free stream conditions |

1 Introduction

For a long time, there has been considerable interest in non-Newtonian fluids. This is because non-Newtonian fluids are found to be of great commercial importance. Examples of such fluids include coal–oil slurries, shampoo, paints, clay coating and suspensions, grease, cosmetic products, custard, physiological liquids (blood, bile, synovial fluid), etc. The classical equations employed in simulating Newtonian viscous flows, i.e. the Navier–Stokes equations fail to simulate a number of critical characteristics of non-Newtonian fluids. Hence several constitutive equations of non-Newtonian fluids have been presented over the past decades. The relationship between the shear stress and rate of strain in such fluids are very complicated in comparison to viscous fluids. The viscoelastic features in non-Newtonian fluids add more complexities in the resulting equations when compared with Navier–Stokes equations. Significant attention has been directed at mathematical and numerical simulation of non-Newtonian fluids. Recent investigations have implemented, respectively, the Casson model [1], second-order Reiner-Rivlin differential fluid models [2], Eringen micro-morphic models [3], Maxwell fluid flow model [4], Carreau fluid model [5], Nanofluid model [6], Williamson Nanofluid model [7] and Jeffery’s viscoelastic fluid model [8].

Convective heat transfer has also mobilized substantial interest owing to its importance in industrial and environmental technologies including energy storage, gas turbines, nuclear plants, rocket propulsion, geothermal reservoirs, photovoltaic panels, etc. The convective boundary condition has also attracted some interest and this usually is simulated via a Biot number in the wall thermal boundary condition. Recently, Ishak [9] discussed the similarity solutions for flow and heat transfer over a permeable surface with convective boundary condition. Aziz [10] provided a similarity solution for laminar thermal boundary layer over a flat surface with a convective surface boundary condition. Aziz [11] further studied hydrodynamic and thermal slip flow boundary layers with an iso-flux thermal boundary condition. The buoyancy effects on thermal boundary layer over a vertical plate subject a convective surface boundary condition was studied by Makinde and Olanrewaju

[12]. Further analyses include Makinde and Aziz [13]. Gupta et al. [14] used a variational finite element to simulate mixed convective-radiative micropolar shrinking sheet flow with a convective boundary condition. Swapna et al. [15] studied convective wall heating effects on hydro-magnetic flow of a micropolar fluid. Makinde et al. [16] studied cross diffusion effects and Biot number influence on hydromagnetic Newtonian boundary layer flow with homogenous chemical reactions and **MAPLE** quadrature routines. Bég et al. [17] analysed Biot number and buoyancy effects on magnetohydrodynamic thermal slip flows. Subhashini et al. [18] studied wall transpiration and cross-diffusion effects on free convection boundary layers with a convective boundary condition. Hayat et al. [19] presented a simple isothermal Nanofluid flow model through a porous space of homogeneous–heterogeneous reactions under the physically acceptable convective type boundary conditions. Ahmad and Mustafa [20] addressed the rotating flow of Nanofluids induced by an exponentially stretching sheet. They implemented the convective boundary conditions to inspect the thermal boundary layer. Junaid et al. [21] considered the three-dimensional rotating flow of Nanofluid induced by a convectively heated deformable surface. They used the shooting approach combined with fifth-order Runge–Kutta method to determine the velocity and temperature distributions above the sheet. Junaid et al. [22] theoretically studied the boundary layer flow of Nanofluid past an exponentially stretching sheet.

An interesting non-Newtonian model developed for chemical engineering systems is the Eyring–Powell fluid model. This rheological model has certain advantages over the other non-Newtonian formulations, including simplicity, ease of computation and physical robustness. Furthermore, it is deduced from kinetic theory of liquids rather than the empirical relation. Additionally, it correctly reduces to Newtonian behavior for low and high shear rates [23]. Several communications utilizing the Eyring–Powell fluid model have been presented in the scientific literature. Hayat et al. [24] numerically studied the chemical reaction and double stratification effects in the flow induced by a nonlinear stretching surface with variable thickness of Eyring–Powell liquid. They examined the heat transfer by considering non-Fourier heat flux model. Najeeb et al. [25] presented the two-layer Eyring–Powell fluid flow in a vertical channel along with nanoparticles using homotopy analysis method. Hayat et al. [26] reported the magnetohydrodynamic boundary layer flow of Powel-Eyring Nanofluid past a non-linear stretching sheet of variable thickness. Khalil-Ur-Rehman et al. [27] analyzed the magnetohydrodynamic boundary layer stagnation point flow of Eyring–Powell fluid induced by an inclined stretching cylindrical surface in the presence of both mixed convection and Joule heating effects using fifth-order Runge–Kutta algorithm

with shooting scheme. Waqas et al. [28] investigated the heat and mass transfer in stagnation point flow of Powell-Eyring liquid due to stretched cylinder using homotopy analysis method. They considered the non-Fourier double-diffusion characteristics that feature the thermal and concentration relaxation factors. Hina et al. [29] explored the peristaltic flow of Eyring–Powell fluid through curved passage with compliant walls in the presence of viscous dissipation and thermophoresis effects using perturbation technique. Hayat et al. [30] investigated the influence of Hall currents on peristaltic transport of conducting Eyring–Powell fluid in an inclined symmetric channel in the presence of Joule heating effect and velocity and thermal slip effects using perturbation technique. Hayat et al. [31] also communicated the magnetohydrodynamic flow of Powell-Eyring nanomaterial bounded by a nonlinear stretching sheet for small magnetic Reynolds number using homotopy analysis method. Other studies on Eyring–Powell fluid include Bhatti et al. [32], Abdul gaffar et al. [33–36].

The objective of the present study was to investigate the laminar boundary layer flow and heat transfer of an Eyring–Powell non-Newtonian fluid from a vertical porous plate. The non-dimensional equations with associated dimensionless boundary conditions constitute a highly nonlinear, coupled two-point boundary value problem. An implicit finite difference “Keller box” scheme is implemented to solve the problem. The effects of the emerging thermophysical parameters, namely the rheological parameters (ϵ, δ), Biot number (γ), Prandtl number (Pr) on the velocity, temperature, local skin friction and heat transfer rate (local Nusselt number) characteristics are studied. The present problem has to the authors’ knowledge not appeared thus far in the scientific literature and is relevant to polymeric manufacturing processes.

2 Non-Newtonian constitutive Eyring–Powell fluid model

In the present study a subclass of non-Newtonian fluids known as the Eyring–Powell fluid is employed owing to its simplicity. Mathematically, the Eyring–Powell model is given as

$$A = -pI + \Gamma, \tag{1}$$

where the extra stress tensor Γ is defined as

$$\Gamma = \mu A_1 + \frac{1}{\beta \dot{\gamma}} \sinh^{-1} \left(\frac{1}{C} \dot{\gamma} \right) A_1 \tag{2}$$

Here μ is dynamic viscosity, β and C are the rheological Eyring–Powell fluid model [37] parameters. Considering the second-order approximation of the \sinh^{-1} function as

$$\sinh^{-1} \left(\frac{1}{C} \dot{\gamma} \right) \cong \frac{1}{C} \dot{\gamma} - \frac{1}{6} \left(\frac{1}{C} \dot{\gamma} \right)^3, \quad \left| \frac{1}{C} \dot{\gamma} \right| \ll 1 \tag{3}$$

Therefore, Eq. (2) takes the form

$$\Gamma = \left(\mu + \frac{1}{\beta C} \right) A_1 - \frac{1}{6\beta C^3} (\dot{\gamma})^2 A_1, \tag{4}$$

where $\dot{\gamma} = \sqrt{\frac{1}{2} \text{tr} A_1^2}$ and the kinematical tensor A_1 is $A_1 = \nabla V + (\nabla V)^T$.

The introduction of the appropriate terms into the flow model is considered next. The resulting boundary value problem is found to be well-posed and permits an excellent mechanism for the assessment of rheological characteristics on the flow behaviour.

3 Mathematical flow model

Steady, double-diffusive, laminar, incompressible, buoyancy-driven convection flow and heat transfer of an Eyring–Powell from a vertical porous plate are illustrated in Fig. 1. Both plate and Eyring–Powell fluid are initially maintained at the same temperature. Instantaneously it is raised to a temperature $T_w (> T_\infty)$, where the latter (ambient) temperature of the fluid remains constant. The x -coordinate is measured from the leading edge of the plate and the y -coordinate is measured normal to the plate. The corresponding velocities in the x and y directions are u and v , respectively. The gravitational acceleration g , acts vertically downwards. The Boussineq approximation holds, i.e. the density variation is only experienced in the buoyancy term in the momentum equation. Introducing the boundary layer approximations, the equations of mass, momentum and energy can be written as follows:

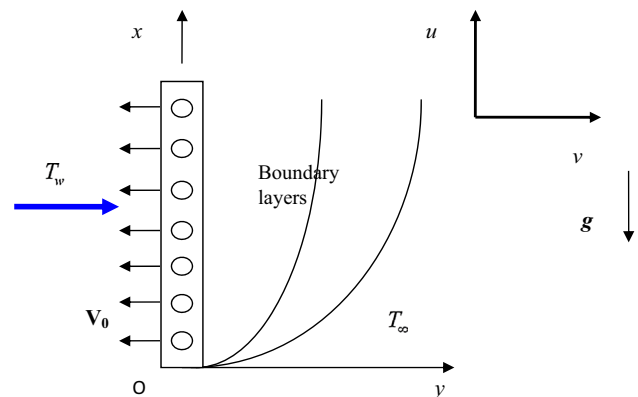


Fig. 1 Physical model

$$\frac{\partial u}{\partial x} + \frac{\partial u}{\partial y} = 0 \quad (5)$$

$$u \frac{\partial u}{\partial x} + v \frac{\partial u}{\partial y} = \left(\nu + \frac{1}{\rho\beta C} \right) \frac{\partial^2 u}{\partial y^2} - \frac{1}{2\rho\beta C^3} \left(\frac{\partial u}{\partial y} \right)^2 \frac{\partial^2 u}{\partial y^2} + g\beta_1(T - T_\infty) \quad (6)$$

$$u \frac{\partial T}{\partial x} + v \frac{\partial T}{\partial y} = \alpha \frac{\partial^2 T}{\partial y^2} \quad (7)$$

The Eyring–Powell fluid model introduces a *mixed* derivative into the momentum boundary layer in Eq. (6). The non-Newtonian effects feature in the shear terms only of Eq. (6) and not the convective (acceleration) terms. The third term on the right-hand side of Eq. (6) represents the *thermal buoyancy force* and couples the velocity field with the temperature field Eq. (7). Viscous dissipation effects are neglected in the model. In Eqs. (5)–(7), u and v are the velocity components in the x and y directions, respectively, and all the parameters are defined in nomenclature.

The appropriate boundary conditions are

$$\begin{aligned} \text{At } y = 0, \quad u = 0, \quad v = -V_w, \quad -k \frac{\partial T}{\partial y} = h_w(T_{w1} - T), \\ \text{As } y \rightarrow \infty, \quad u \rightarrow 0, \quad T \rightarrow T_\infty \end{aligned} \quad (8)$$

where V_w denotes the uniform transpiration (blowing or suction) velocity at the surface of the vertical plate, k is the thermal conductivity, h_w is the convective heat transfer coefficient and T_{w1} is the convective fluid temperature. To transform the boundary value problem to a dimensionless one, we introduce a stream function ψ defined by the Cauchy–Riemann equations, $u = \frac{\partial \psi}{\partial y}$ and $v = -\frac{\partial \psi}{\partial x}$, and therefore, the mass conservation Eq. (5) is automatically satisfied. In order to render the governing equations and the boundary conditions in dimensionless form, the following dimensionless variables are introduced into Eqs. (6), (7) and (8):

$$\begin{aligned} \xi = \frac{V_0 x}{\nu} Gr_x^{-1/4}, \quad \eta = \frac{y}{x} Gr_x^{1/4}, \\ \psi = 4\nu Gr_x^{1/4} \left(f(\xi, \eta) + \frac{1}{4}\xi \right), \quad \theta(\xi, \eta) = \frac{T - T_\infty}{T_w - T_\infty} \\ \text{Pr} = \frac{\nu}{\alpha}, \quad Gr_x = \frac{g\beta_1(T_w - T_\infty)x^3}{4\nu^2}, \\ \varepsilon = \frac{1}{\mu\beta C}, \quad \delta = \frac{8\nu^2}{C^2 x^4} Gr_x^{3/2} \end{aligned} \quad (9)$$

The resulting momentum and energy boundary layer equations take the following form:

$$\begin{aligned} (1 + \varepsilon)f''' + (3f + \xi)f'' - 2(f')^2 + \theta - \varepsilon\delta(f'')^2 f''' \\ = \xi \left(f' \frac{\partial f'}{\partial \xi} - f'' \frac{\partial f}{\partial \xi} \right) \end{aligned} \quad (10)$$

$$\frac{\theta''}{\text{Pr}} + (3f + \xi)\theta' = \xi \left(f' \frac{\partial \theta}{\partial \xi} - \theta' \frac{\partial f}{\partial \xi} \right) \quad (11)$$

The corresponding non-dimensional boundary conditions for the collectively fifth order, multi-degree partial differential equation system defined by Eqs. (10), (11) assume the following form:

$$\begin{aligned} \text{At } \eta = 0, \quad f = f_w, \quad f' = 0, \quad \theta = 1 + \frac{\theta'}{\gamma} \\ \text{As } \eta \rightarrow \infty, \quad f' \rightarrow 0, \quad \theta \rightarrow 0 \end{aligned} \quad (12)$$

Here primes denote the differentiation with respect to η . $\gamma = \frac{xh_{w1}}{k} Gr_x^{-1/4}$ is the Biot number. $f_w = \frac{-V_w x}{3\nu \sqrt[4]{Gr_x}}$ is the suction/injection parameter. The wall thermal boundary condition in (12) corresponds to convective cooling. The skin-friction coefficient (shear stress at the Plate surface) and Nusselt number (heat transfer rate) can be defined using the transformations described above with the following expressions:

$$Gr_x^{-3/4} C_f = (1 + \varepsilon)f''(\xi, 0) - \frac{\varepsilon}{3}\delta(f''(\xi, 0))^3 \quad (13)$$

$$Gr_x^{-1/4} Nu = -\theta'(\xi, 0) \quad (14)$$

The location, $\xi \sim 0$, corresponds to the vicinity of the *lower stagnation point* on the plate. For this scenario, the model defined by Eqs. (10), (11) contracts to an *ordinary* differential boundary value problem:

$$(1 + \varepsilon)f'''' + 3ff'' - 2(f')^2 + \theta - \varepsilon\delta(f'')^2 f'''' = 0 \quad (15)$$

$$\frac{\theta''}{\text{Pr}} + 3f\theta' = 0 \quad (16)$$

The general model is solved using a powerful and unconditionally stable finite difference technique introduced by Keller [38]. The Keller-box method has a second-order accuracy with arbitrary spacing and attractive extrapolation features.

4 Numerical solution with Keller box implicit method

The Keller-Box implicit difference method is implemented to solve the nonlinear boundary value problem defined by Eqs. (10), (11) with boundary conditions (12). This technique, despite recent developments in other numerical methods, remains a powerful and very accurate approach for parabolic boundary layer flows. It is unconditionally stable and achieves exceptional accuracy [38]. Recently this method has been deployed in

resolving many challenging, multi-physical fluid dynamics problems. These include magnetohydrodynamics applications of Keller’s method reviewed in Bég [39], micropolar Nanofluid transport from a horizontal circular cylinder [40], Nanofluid transport from a sphere [41], Walter’s B viscoelastic flows [42], hyperbolic-tangent convection flows from curved bodies [43], Jeffrey’s elasto-viscous boundary layers [44] and magnetic Williamson fluids [45]. The Keller-Box discretization is *fully coupled* at each step which reflects the physics of parabolic systems—which are also fully coupled. Discrete calculus associated with the Keller-Box scheme has also been shown to be fundamentally different from all other mimetic (physics capturing) numerical methods, as elaborated by Keller [38]. The Keller Box Scheme comprises four stages.

1. Reduction of the N th order partial differential equation system to N first-order Equations.
2. Finite Difference Discretization.
3. Quasilinearization of Non-Linear Keller Algebraic Equations.
4. Block-tridiagonal Elimination of Linear Keller Algebraic Equations.

Step 1: Reduction of the N th order partial differential equation system to N first order equations

Equations (8)–(9) subject to the boundary conditions (10) are first cast as a multiple system of first order differential equations. New dependent variables are introduced:

$$u(x, y) = f', \quad v(x, y) = f'', \quad s(x, y) = \theta, \quad t(x, y) = \theta' \quad (17)$$

These denote the variables for velocity, temperature and concentration, respectively. Now Eqs. (10), (11) are solved as a set of fifth-order simultaneous differential equations:

$$f' = u \quad (18)$$

$$u' = v \quad (19)$$

$$\theta' = t \quad (20)$$

$$(1 + \varepsilon)v' + (3f + \xi)v - 2u^2 + s - \varepsilon\delta v^2 v' = \xi \left(u \frac{\partial u}{\partial \xi} - v \frac{\partial f}{\partial \xi} \right) \quad (21)$$

$$\frac{t'}{\text{Pr}} + (3f + \xi)t = \xi \left(u \frac{\partial s}{\partial \xi} - t \frac{\partial f}{\partial \xi} \right), \quad (22)$$

where primes denote differentiation with respect to η . In terms of the dependent variables, the boundary conditions become

$$\begin{aligned} \text{At } \eta = 0, \quad & f = 0, \quad f' = 0, \quad \theta = 1 + \frac{\theta'}{\gamma} \\ \text{As } \eta \rightarrow \infty, \quad & f' \rightarrow 0, \quad \theta \rightarrow 0 \end{aligned} \quad (23)$$

Step 2: Finite difference discretization

A two-dimensional computational grid is imposed on the ξ - η plane as sketched in Fig. 2. The stepping process is defined by

$$\eta_0 = 0, \quad \eta_j = \eta_{j-1} + h_j, \quad j = 1, 2, \dots, J, \quad \eta_J \equiv \eta_\infty \quad (24)$$

$$\xi^0 = 0, \quad \xi^n = \xi^{n-1} + k_n, \quad n = 1, 2, \dots, N, \quad (25)$$

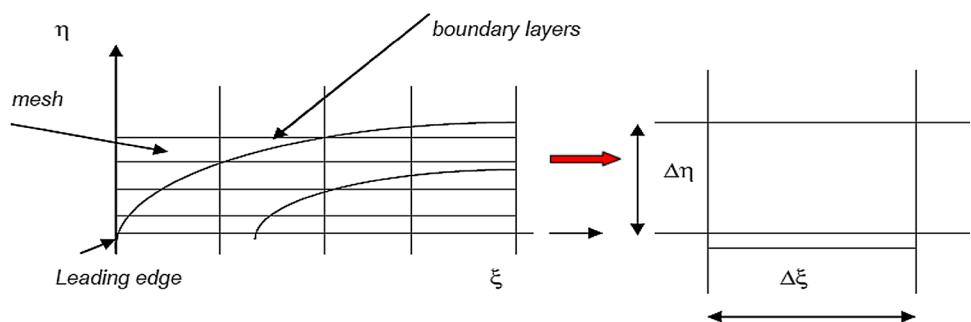
where k_n and h_j denote the step distances in the ξ and η directions, respectively. If g_j^n denotes the value of any variable at (η_j, ξ^n) , then the variables and derivatives of Eqs. (18)–(22) at $(\eta_{j-1/2}, \xi^{n-1/2})$ are replaced by

$$g_{j-1/2}^{n-1/2} = \frac{1}{4} (g_j^n + g_{j-1}^n + g_j^{n-1} + g_{j-1}^{n-1}) \quad (26)$$

$$\left(\frac{\partial g}{\partial \eta} \right)_{j-1/2}^{n-1/2} = \frac{1}{2h_j} (g_j^n - g_{j-1}^n + g_j^{n-1} - g_{j-1}^{n-1}) \quad (27)$$

$$\left(\frac{\partial g}{\partial \xi} \right)_{j-1/2}^{n-1/2} = \frac{1}{2k^n} (g_j^n - g_{j-1}^n + g_j^{n-1} - g_{j-1}^{n-1}) \quad (28)$$

Fig. 2 Grid meshing and a Keller box computational cell



The resulting finite-difference approximation of Eqs. (18)–(22) for the mid-point $(\eta_{j-1/2}, \xi^n)$, takes the following form:

$$h_j^{-1} (f_j^n - f_{j-1}^n) = u_{j-1/2}^n \tag{29}$$

$$h_j^{-1} (u_j^n - u_{j-1}^n) = v_{j-1/2}^n \tag{30}$$

$$h_j^{-1} (\theta_j^n - \theta_{j-1}^n) = t_{j-1/2}^n \tag{31}$$

$$\begin{aligned} (1 + \varepsilon)(v_j - v_{j-1}) + (3 + \alpha) \frac{h_j}{4} (f_j + f_{j-1})(v_j + v_{j-1}) \\ + \xi \frac{h_j}{2} (v_j + v_{j-1}) - (2 + \alpha) \frac{h_j}{4} (u_j + u_{j-1})^2 \\ + \frac{h_j}{2} (s_j + s_{j-1}) - \frac{\varepsilon \delta}{4} (v_j + v_{j-1})^2 (v_j - v_{j-1}) \\ + \frac{\alpha h_j}{2} v_{j-1}^{n-1} (f_j + f_{j-1}) - \frac{\alpha h_j}{2} f_{j-1}^{n-1} (v_j + v_{j-1}) = [R_1]_{j-1/2}^{n-1} \end{aligned} \tag{32}$$

$$\begin{aligned} \frac{1}{Pr} (t_j - t_{j-1}) + \frac{(3 + \alpha) h_j}{4} (f_j + f_{j-1})(t_j + t_{j-1}) \\ + \xi \frac{h_j}{2} (t_j + t_{j-1}) - \frac{\alpha h_j}{4} (u_j + u_{j-1})(s_j + s_{j-1}) \\ + \frac{\alpha h_j}{2} s_{j-1}^{n-1} (u_j + u_{j-1}) - \frac{\alpha h_j}{2} u_{j-1/2}^{n-1} (s_j + s_{j-1}) \\ - \frac{\alpha h_j}{2} f_{j-1/2}^{n-1} (t_j + t_{j-1}) + \frac{\alpha h_j}{2} t_{j-1/2}^{n-1} (f_j + f_{j-1}) = [R_2]_{j-1/2}^{n-1}, \end{aligned} \tag{33}$$

where the following notation applies:

$$\alpha = \frac{\xi^{n-1/2}}{k_n} \tag{34}$$

$$[R_1]_{j-1/2}^{n-1} = -h_j \left[\begin{aligned} &(1 + \varepsilon)(v')_{j-1/2}^{n-1} + (3 - \alpha) f_{j-1/2}^{n-1} v_{j-1/2}^{n-1} \\ &+ \xi v_{j-1/2}^{n-1} - (2 - \alpha) (u_{j-1/2}^{n-1})^2 \\ &+ s_{j-1/2}^{n-1} - \varepsilon \delta (v^2)_{j-1/2}^{n-1} (v')_{j-1/2}^{n-1} \end{aligned} \right] \tag{35}$$

$$\begin{aligned} [R_2]_{j-1/2}^{n-1} = -h_j \left[\frac{1}{Pr} (t')_{j-1/2}^{n-1} + (3 - \alpha) f_{j-1/2}^{n-1} t_{j-1/2}^{n-1} \right. \\ \left. + \xi t_{j-1/2}^{n-1} + \alpha u_{j-1/2}^{n-1} s_{j-1/2}^{n-1} \right] \end{aligned} \tag{36}$$

The boundary conditions are

$$f_0^n = u_0^n = 0, \quad s_0^n = 1, \quad u_J^n = 0, \quad v_J^n = 0, \quad s_J^n = 0 \tag{37}$$

Step 3: Quasilinearization of non-linear Keller algebraic equations

Assuming $f_j^{n-1}, u_j^{n-1}, v_j^{n-1}, s_j^{n-1}, t_j^{n-1}$ to be known for $0 \leq j \leq J$, then Eqs. (29)–(33) constitute a system of

$5J + 5$ equations for the solution of $5J + 5$ unknowns $f_j^n, u_j^n, v_j^n, s_j^n, t_j^n, \quad j = 0, 1, 2, \dots, J$. This non-linear system of algebraic equations is linearized by means of Newton’s method as explained in Keller [38] and Prasad [46].

Step 4: Block-tridiagonal elimination of linear Keller algebraic equations

The linearized system is solved by the *block-elimination* method owing to its *block-tridiagonal* structure. The block-tridiagonal structure generated consists of *block matrices*. The complete linearized system is formulated as a *block matrix system*, where each element in the coefficient matrix is a matrix itself, and this system is solved using the efficient Keller-box method. The numerical results are strongly influenced by the number of mesh points in both directions. After some trials in the η -direction (radial coordinate) a larger number of mesh points are selected, whereas in the ξ -direction (tangential coordinate) significantly less mesh points are necessary. η_{\max} has been set at 15 and this constitutes an adequately large value at which the prescribed boundary conditions are satisfied. ξ_{\max} is set at 3.0 for the simulations. *Mesh independence* has been comfortably attained in the simulations. The numerical algorithm is executed in **MATLAB** on a PC. The method demonstrates excellent stability, convergence and consistency, as elaborated by Keller [38].

5 Numerical results and interpretation

Comprehensive solutions have been obtained and are presented in Tables 1, 2, 3, 4, 5 and Figs. 3, 4, 5, 6, 7, 8. The numerical problem comprises two independent variables (ξ, η) , two dependent fluid dynamic variables (f, θ) and five thermo-physical and body force control parameters, namely $\varepsilon, \delta, \gamma, Pr, \xi$. The following default parameter values, i.e. $\varepsilon = 0.1, \delta = 0.1, \gamma = 0.3, Pr = 0.71, \xi = 1.0$ are prescribed (unless otherwise stated). Furthermore, the influence of stream-wise (transverse) coordinate on heat transfer characteristics is also investigated.

In Tables 1, 2, we present the influence of the Eyring–Powell fluid parameter, ε , on the skin friction and heat transfer rate, along with a variation in Prandtl number (Pr). With increasing ε , the skin friction is enhanced. The parameter ε is inversely proportional to the dynamic viscosity of the non-Newtonian fluid. There as ε is elevated, viscosity will be reduced and this will induce lower resistance to the flow at the surface of the plate, i.e. accelerate the flow leading to an *escalation* of shear stress. Furthermore, this trend is sustained at any Prandtl number. However, an increase in Prandtl number markedly reduces the shear stress magnitudes. Similarly increasing ε is observed to reduce heat transfer rates, again at all Prandtl numbers, whereas it strongly accentuates heat transfer rates. Magnitudes of

Table 1 Values of $f''(\xi, 0)$ and $-\theta'(\xi, 0)$ for different ε and Pr ($\delta = 0.1, \gamma = 0.3, \xi = 1.0$)

| Pr | $\varepsilon = 0.0$ | | $\varepsilon = 0.3$ | | $\varepsilon = 0.5$ | | $\varepsilon = 0.7$ | |
|------|---------------------|--------------------|---------------------|--------------------|---------------------|--------------------|---------------------|--------------------|
| | $f''(\xi, 0)$ | $-\theta'(\xi, 0)$ | $f''(\xi, 0)$ | $-\theta'(\xi, 0)$ | $f''(\xi, 0)$ | $-\theta'(\xi, 0)$ | $f''(\xi, 0)$ | $-\theta'(\xi, 0)$ |
| 0.5 | 2.0500 | 0.3784 | 2.1366 | 0.3723 | 2.1872 | 0.3689 | 2.2334 | 0.3659 |
| 0.7 | 1.8007 | 0.4866 | 1.8678 | 0.4796 | 1.9068 | 0.4758 | 1.9422 | 0.4724 |
| 1.0 | 1.5449 | 0.6336 | 1.5935 | 0.6264 | 1.6214 | 0.6225 | 1.6465 | 0.6230 |
| 2.0 | 1.0104 | 1.1533 | 1.0262 | 1.1493 | 1.0344 | 1.1475 | 1.0409 | 1.1451 |
| 3.0 | 0.7197 | 1.6973 | 0.7212 | 1.6971 | 0.7218 | 1.6963 | 0.7242 | 1.6972 |
| 5.0 | 0.4314 | 2.8157 | 0.4328 | 2.8210 | 0.4323 | 2.8224 | 0.4315 | 2.8251 |
| 7.0 | 0.3045 | 3.9433 | 0.3044 | 3.9486 | 0.3044 | 3.9538 | 0.3051 | 3.9585 |
| 10.0 | 0.2075 | 5.6483 | 0.2079 | 5.6515 | 0.2085 | 5.6542 | 0.2091 | 5.6569 |

Table 2 Values of $f''(\xi, 0)$ and $-\theta'(\xi, 0)$ for different ε and Pr ($\delta = 0.1, \gamma = 0.3, \xi = 1.0$)

| Pr | $\varepsilon = 1.0$ | | $\varepsilon = 2.0$ | | $\varepsilon = 5.0$ | |
|------|---------------------|--------------------|---------------------|--------------------|---------------------|--------------------|
| | $f''(\xi, 0)$ | $-\theta'(\xi, 0)$ | $f''(\xi, 0)$ | $-\theta'(\xi, 0)$ | $f''(\xi, 0)$ | $-\theta'(\xi, 0)$ |
| 0.5 | 2.2961 | 0.3619 | 2.4648 | 0.3517 | 2.7865 | 0.3359 |
| 0.7 | 1.9899 | 0.4680 | 2.1163 | 0.4595 | 2.3431 | 0.4496 |
| 1.0 | 1.6751 | 0.6295 | 1.7648 | 0.5955 | 1.9066 | 0.5899 |
| 2.0 | 1.0492 | 1.1435 | 1.0677 | 1.1400 | 1.0821 | 1.1371 |
| 3.0 | 0.7260 | 1.6965 | 0.7271 | 1.6998 | 0.7261 | 1.7018 |
| 5.0 | 0.4306 | 2.8266 | 0.4338 | 2.8332 | 0.4323 | 2.8395 |
| 7.0 | 0.3057 | 3.9631 | 0.3045 | 3.9639 | 0.3087 | 3.9742 |
| 10.0 | 0.2091 | 5.6569 | 0.2116 | 5.6704 | 0.2126 | 5.6746 |

Table 3 Values of $f''(\xi, 0)$ and $-\theta'(\xi, 0)$ for different δ and Pr ($\delta = 0.1, \gamma = 0.3, \xi = 1.0$)

| Pr | $\delta = 0.0$ | | $\delta = 5$ | | $\delta = 10$ | |
|------|----------------|--------------------|---------------|--------------------|---------------|--------------------|
| | $f''(\xi, 0)$ | $-\theta'(\xi, 0)$ | $f''(\xi, 0)$ | $-\theta'(\xi, 0)$ | $f''(\xi, 0)$ | $-\theta'(\xi, 0)$ |
| 0.5 | 1.9715 | 0.2356 | 1.9609 | 0.2361 | 1.9492 | 0.2367 |
| 0.7 | 1.8527 | 0.2753 | 1.8442 | 0.2759 | 1.8350 | 0.2765 |
| 1.0 | 1.7337 | 0.3213 | 1.7271 | 0.3219 | 1.7199 | 0.3225 |
| 2.0 | 1.4870 | 0.4462 | 1.4833 | 0.4468 | 1.4793 | 0.4474 |
| 3.0 | 1.3399 | 0.5500 | 1.3374 | 0.5504 | 1.3347 | 0.5511 |
| 5.0 | 1.1515 | 0.7364 | 1.1501 | 0.7368 | 1.1486 | 0.7373 |
| 7.0 | 1.0253 | 0.9133 | 1.0244 | 0.9136 | 1.0235 | 0.9139 |
| 10.0 | 0.8900 | 1.1759 | 0.8895 | 1.1761 | 0.8890 | 1.1763 |

Table 4 Values of $f''(\xi, 0)$ and $-\theta'(\xi, 0)$ for different δ and Pr ($\delta = 0.1, \gamma = 0.3, \xi = 1.0$)

| Pr | $\delta = 15$ | | $\delta = 20$ | | $\delta = 25$ | |
|------|---------------|--------------------|---------------|--------------------|---------------|--------------------|
| | $f''(\xi, 0)$ | $-\theta'(\xi, 0)$ | $f''(\xi, 0)$ | $-\theta'(\xi, 0)$ | $f''(\xi, 0)$ | $-\theta'(\xi, 0)$ |
| 0.5 | 1.9362 | 0.2373 | 1.9210 | 0.2380 | 1.9016 | 0.2390 |
| 0.7 | 1.8249 | 0.2771 | 1.8135 | 0.2779 | 1.8001 | 0.2788 |
| 1.0 | 1.7122 | 0.3232 | 1.7037 | 0.3239 | 1.3940 | 0.3248 |
| 2.0 | 1.4751 | 0.4480 | 1.4706 | 0.4487 | 1.4658 | 0.4495 |
| 3.0 | 1.3319 | 0.5516 | 1.3290 | 0.5523 | 1.3259 | 0.5529 |
| 5.0 | 1.1471 | 0.7378 | 1.1456 | 0.7382 | 1.1440 | 0.7387 |
| 7.0 | 1.0226 | 0.9143 | 1.0217 | 0.9147 | 1.0207 | 0.9150 |
| 10.0 | 0.8885 | 1.1765 | 0.8881 | 1.1767 | 0.8876 | 1.1769 |

Table 5 Numerical Values of $f''(\xi, 0)$ (in brackets) and skin friction coefficient C_f for different values of δ and ε

| $\delta \varepsilon$ | 0.0 | 0.2 | 0.4 | 0.6 | 0.8 | 1.0 |
|----------------------|--------|--------------------|--------------------|--------------------|--------------------|--------------------|
| 0.0 | 1.8001 | 1.9019 (1.5849) | 1.9918 (1.4227) | 2.0728 (1.2955) | 2.1466 (1.1926) | 2.2146 (1.1073) |
| 0.1 | 1.8001 | 1.9016 (1.5860) | 1.9915 (1.4242) | 2.0724 (1.2969) | 2.1462 (1.1939) | 2.2141 (1.1085) |
| 0.2 | 1.8001 | 1.9013 (1.5872) | 1.9911 (1.4256) | 2.0719 (1.2984) | 2.1457 (1.1952) | 2.2137 (1.1097) |
| 0.3 | 1.8001 | 1.9010 (1.5884) | 1.9907 (1.4271) | 2.0715 (1.2998) | 2.1452 (1.1966) | 2.2132 (1.1109) |
| 0.4 | 1.8001 | 1.9008 (1.5896) | 1.9903 (1.4286) | 2.0710 (1.3013) | 2.1448 (1.1979) | 2.2128 (1.1121) |
| 0.5 | 1.8001 | 1.9005 (1.5907) | 1.9899 (1.4300) | 2.0706 (1.3028) | 2.1443 (1.1993) | 2.2123 (1.1133) |
| 0.6 | 1.8001 | 1.9002 (1.5919) | 1.9895 (1.4315) | 2.0702 (1.3042) | 2.1439 (1.2007) | 2.2118 (1.1146) |
| 0.7 | 1.8001 | 1.8999 (1.5931) | 1.9891 (1.4330) | 2.0697 (1.3057) | 2.1434 (1.2020) | 2.2114 (1.1158) |
| 0.8 | 1.8001 | 1.8997 (1.5943) | 1.9887 (1.4346) | 2.0693 (1.3072) | 2.1429 (1.2034) | 2.2109 (1.1171) |
| 0.9 | 1.8001 | 1.8994 (1.5955) | 1.9883 (1.4361) | 2.0688 (1.3088) | 2.1425 (1.2048) | 2.2104 (1.1183) |
| 1.0 | 1.8001 | 1.8991 (1.5967) | 1.9879 (1.4376) | 2.0684 (1.3103) | 2.1420 (1.2063) | 2.2100 (1.1196) |

shear stress are always positive indicating that flow reversal (backflow) never arises.

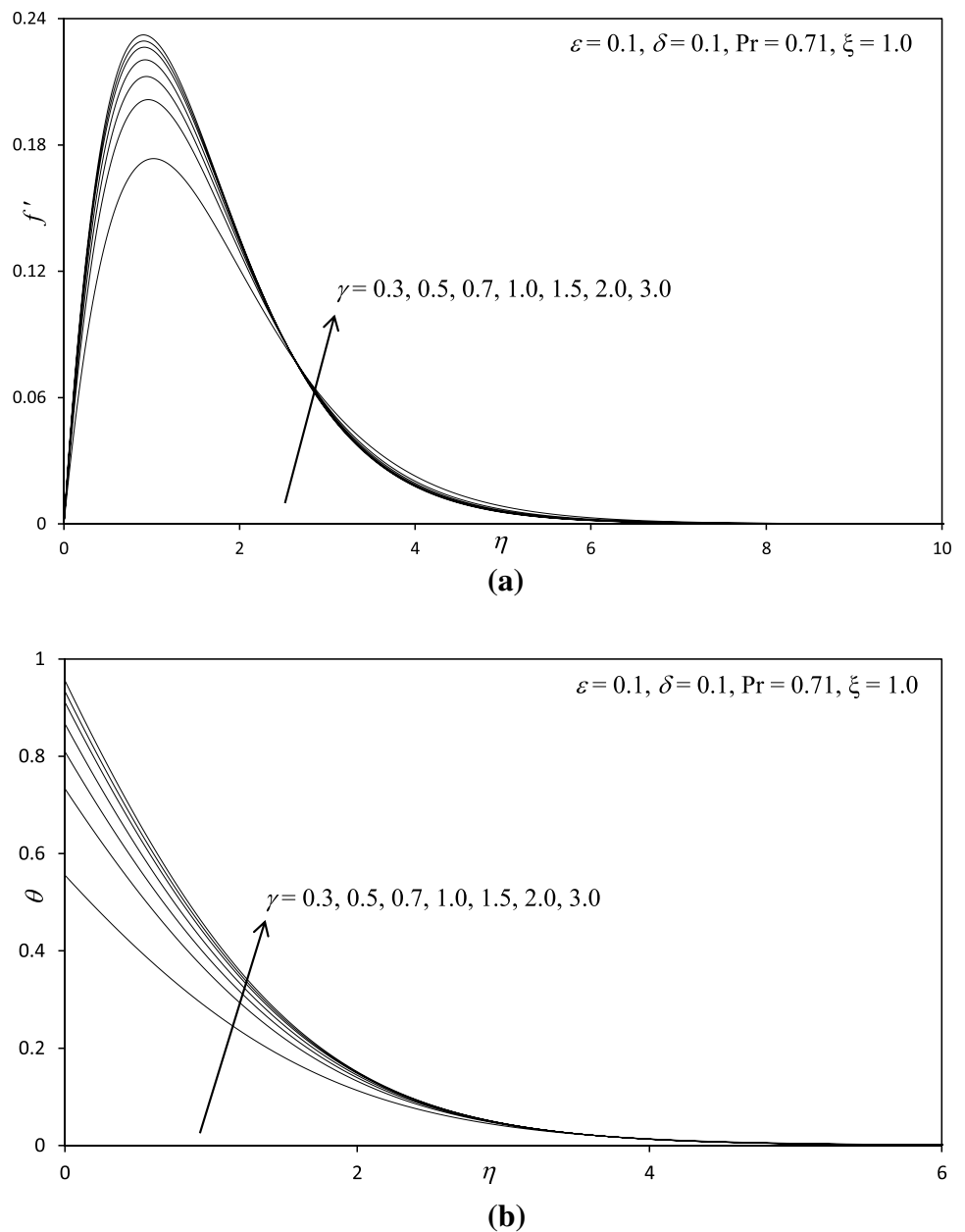
Tables 3, 4 document results for the influence of the local non-Newtonian parameter (based on length scale x), i.e. δ and also the Prandtl number (Pr) on skin friction and heat transfer rate. Skin friction is generally decreased with increasing δ . However, heat transfer rate (i.e. local Nusselt number function) is found to be enhanced with increasing δ . $\delta = \frac{8\nu^2}{C^2 x^4} Gr_x^{3/2}$ and inspection of this definition shows that the direct proportionality of δ to kinematic viscosity (ν) (with all other parameters being maintained constant) will generate a strong resistance to the flow leading to a deceleration. i.e. drop in shear stresses. Conversely, the direct proportionality of δ to Grashof number (Gr) will imply that thermal buoyancy forces are enhanced as δ increases, and this will cause a boost in heat transfer by convection from the plate surface manifesting with the greater heat transfer rates observed in Tables 3 and 4. These tables also show that with an increase in the Prandtl number, Pr, the skin friction is also depressed, whereas the heat transfer rate is elevated.

Table 5 presents the Keller box numerical values of the missing condition $f''(\xi, 0)$ (in brackets) and skin friction C_f for various values of δ and ε . It is found that skin friction is reduced with increasing values of δ . Furthermore, the skin friction C_f is observed to be increased with a rise in the Eyring–Powell fluid parameter (ε) for all values of the local non-Newtonian parameter (δ).

Table 6 shows the comparison values of the present study with those obtained by Hossain et al. [47] for natural convection heat transfer along a vertical porous plate and are found to be in excellent agreement.

Figure 3a, b depicts the evolution of velocity (f') and temperature (θ) functions with a variation in Biot number, γ . Dimensionless velocity component (Fig. 3a) is considerably enhanced with increasing γ . In Fig. 3b, an increase in Biot number is also seen to considerably enhance temperature throughout the boundary layer regime. For $\gamma < 1$, i.e. small Biot numbers, the regime is frequently designated as being “thermally simple” and there is a presence of more uniform temperature fields inside the boundary layer and the plate surface. For $\gamma > 1$ thermal fields are anticipated to be non-uniform within the solid body. The Biot number effectively furnishes a mechanism for comparing the conduction resistance within a solid body to the convection resistance external to that body (offered by the surrounding fluid) for heat transfer. We also note that a Biot number in excess of 0.1, as studied in Fig. 3a, b, corresponds to a “thermally thick” substance, whereas Biot number less than 0.1 implies a “thermally thin” material. Since γ is inversely proportional to thermal conductivity (k), as γ increases, thermal conductivity will be reduced at the plate surface and this will lead to a decrease in the rate of heat transfer from the boundary layer to within the plate, manifesting in a rise in temperature at the plate surface and in the body of the fluid the maximum effect will be sustained at the surface, as witnessed in Fig. 3b. However for a fixed wall

Fig. 3 **a** Influence of γ on velocity profiles, **b** influence of γ on temperature profiles



convection coefficient and thermal conductivity, Biot number as defined in $\gamma = \frac{xh_w}{k} Gr_x^{-1/4}$ is also directly inversely proportional to the local Grashof (free convection) number. As local Grashof number increases generally the enhancement in buoyancy causes a deceleration in boundary layer flows; however, as Biot number increases, the local Grashof number must decrease and this will induce the opposite effect, i.e. accelerate the boundary layer flow, as shown in Fig. 3a.

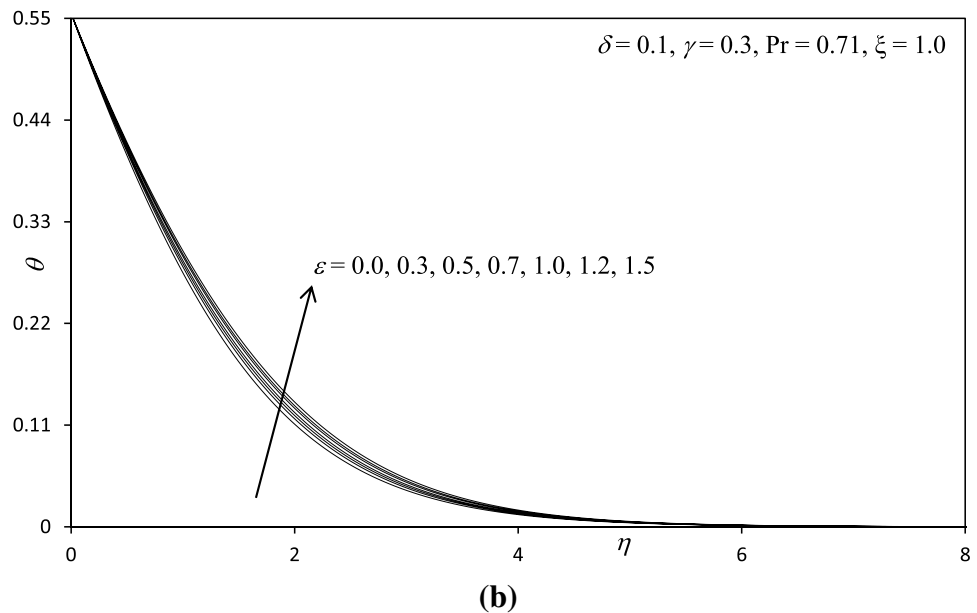
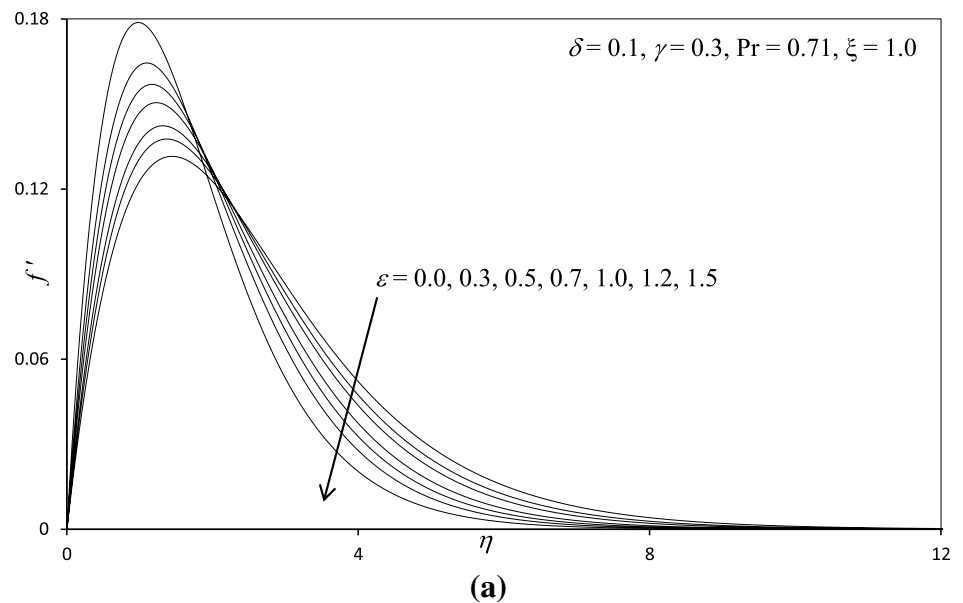
Figure 4a, b illustrates the effect of Eyring–Powell fluid parameter ε , on the velocity (f') and temperature (θ) distributions through the boundary layer regime. Velocity is significantly decreased with increasing ε at larger distance from the plate surface owing to the simultaneous

drop in dynamic viscosity. Conversely, temperature is consistently enhanced with increasing values of ε . The mathematical model reduces to the *Newtonian viscous flow model* as $\varepsilon \rightarrow 0$ and $\delta \rightarrow 0$. The momentum boundary layer equation in this case contracts to the familiar equation for *Newtonian mixed convection* from a plate, viz

$$f''' + (3f + \xi)f'' - 2(f')^2 + \theta = \xi \left(f' \frac{\partial f'}{\partial \xi} - f'' \frac{\partial f}{\partial \xi} \right). \quad (38)$$

The thermal boundary layer Eq. (9) remains unchanged. In Fig. 4b, temperatures are clearly minimized for the Newtonian case ($\varepsilon = 0$) and maximized for the strongest non-Newtonian case ($\varepsilon = 1.0$). The non-Newtonian parameter

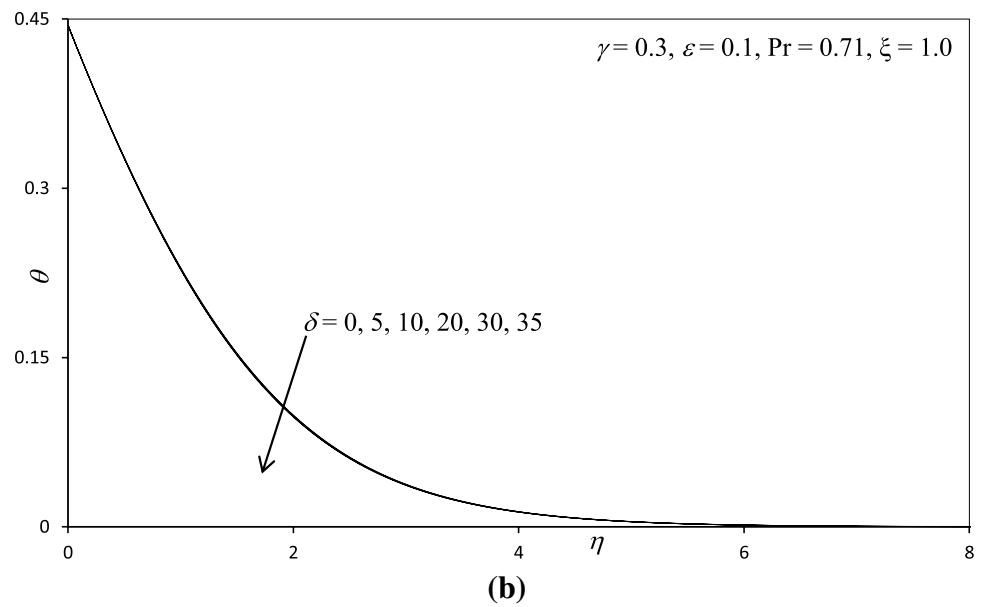
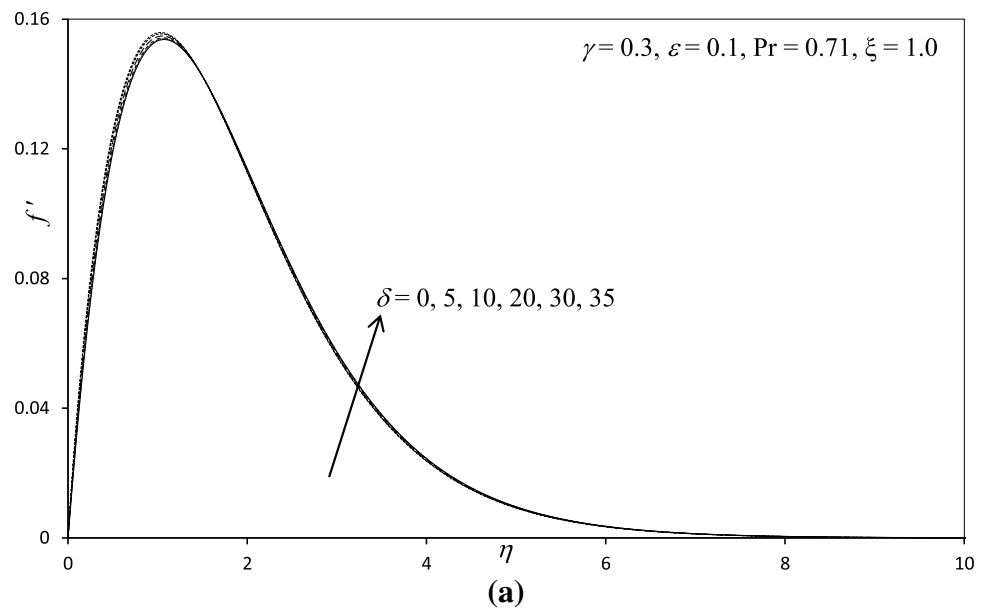
Fig. 4 **a** Influence of ε on velocity profiles, **b** influence of ε on temperature profiles



ε ($=1/[\mu\beta C]$) is evidently inversely proportional to the viscosity and also to β and C (Eyring–Powell rheological fluid parameters). As ε is increased, the material viscosity, therefore, will decrease which would aid momentum development. Similarly the parameters β and C are simultaneously reduced (they are strongly linked to viscosity) and the overall effect is a boost in material viscosity. This results in reduction in the ε magnitude which manifests in marked deceleration in the flow as shown in Fig. 4a. With decreased momentum diffusion rates the velocity boundary layer thickness is decreased. Thermal diffusion is conversely enhanced and the fluid heated (Fig. 4b), resulting in a thickening in the thermal boundary layer.

Figure 5a, b depicts the velocity (f') and temperature (θ) distributions with increasing local non-Newtonian fluid parameter δ . Very little tangible effect is observed in Fig. 5a, although there is a very slight increase in velocity with increase in δ . Similarly, there is only a very slight depression in temperature magnitudes in Fig. 5b with a rise in δ . This parameter is defined as $v^2 \text{Re}_x^3 / (2C^2 x^4)$, features in a single negative term in Eq. (8), viz, $-\varepsilon \delta (f'')^2 f'''$, unlike ε , rheological parameter which also appears in the shear term, $-(1 + \varepsilon)^2 f'''$. This parameter also features viscosity which effectively is decreased weakly and induces a slight acceleration in the flow. Therefore, the momentum boundary layer thickness is decreased slightly,

Fig. 5 **a** Influence of δ on velocity profiles, **b** influence of δ on temperature profiles

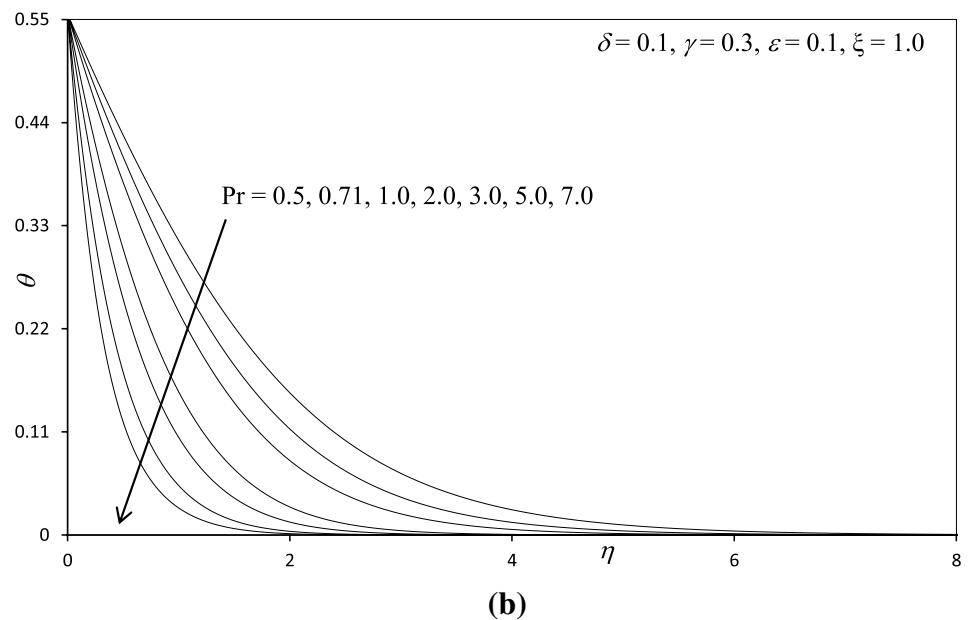
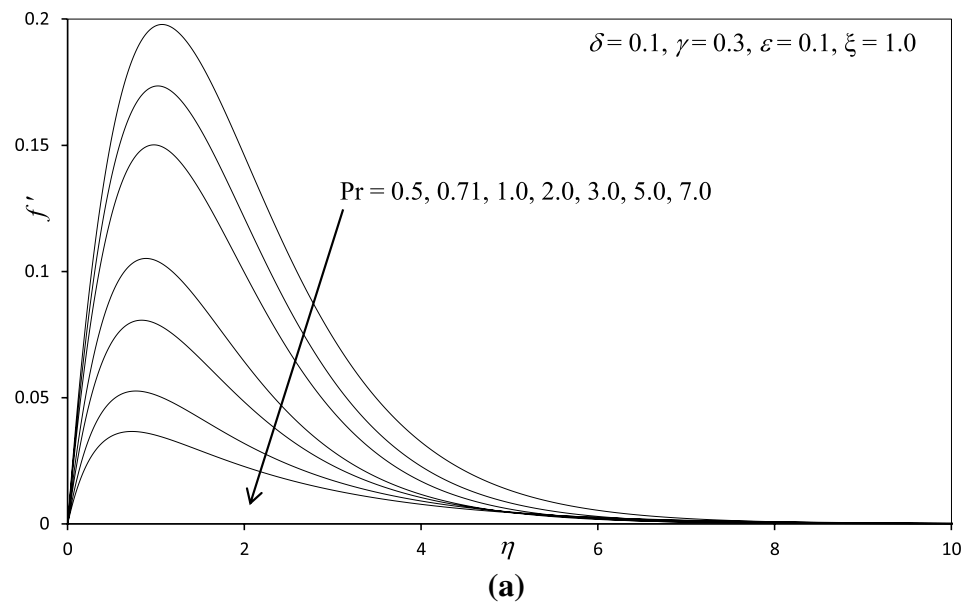


whereas the thermal boundary layer thickness is marginally reduced.

Figure 6a, b depicts the profiles for velocity (f') and temperature (θ) for various values of Prandtl number, Pr. It is observed that an increase in the Prandtl number significantly decelerates the flow, i.e. velocity decreases. Also increasing Prandtl number is found to decelerate the temperature. The solutions to denser fluids, i.e. water-based solvents, very low-density spray paints [48], etc. Prandtl number must be varied, as this is the only non-dimensional parameter which categorizes thermofluid properties. For example, $Pr = 5$ corresponds closely to actual characteristics for chlorofluorocarbon

halomethane (CFC) which is used in aerosol spray propellants. $Pr = 7$ represents certain paint-thinners as well as water at room temperature. Prandtl number defines the ratio of viscous diffusion to thermal diffusion in the boundary layer regime. For $Pr > 1$, momentum diffusivity will exceed thermal diffusivity, but for $Pr < 1$, thermal diffusivity will exceed momentum diffusivity. Increasing Pr is known to significantly depress temperatures in the boundary layer, as elaborated in Incropera and DeWitt [49] and Schlichting [50]. Pr signifies the ratio of momentum diffusivity to thermal diffusivity. Pr is the most important parameter in heat transfer analysis as it corresponds to actual physical properties of fluids

Fig. 6 **a** Influence of Pr on velocity profiles, **b** influence of Pr on temperature profiles

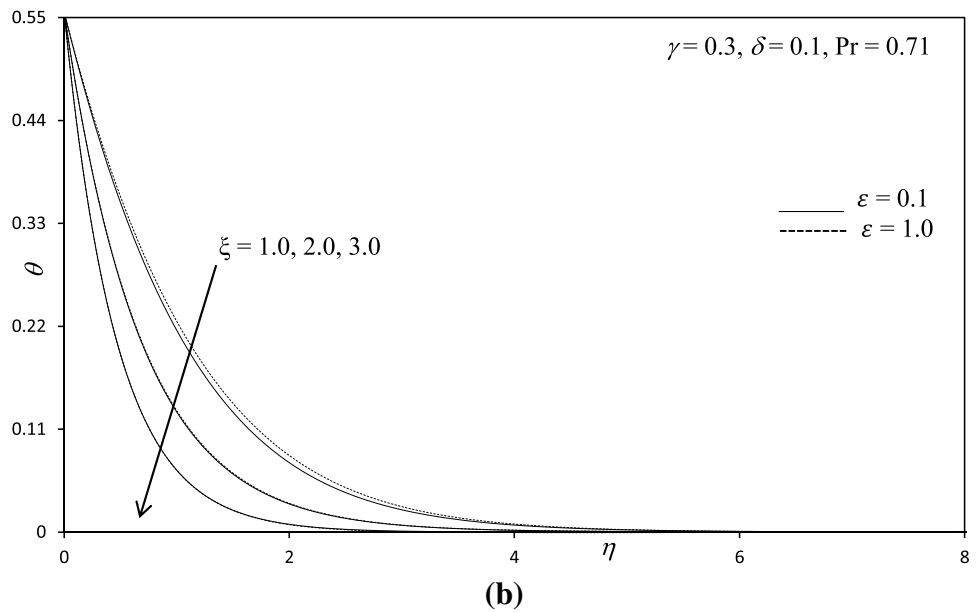
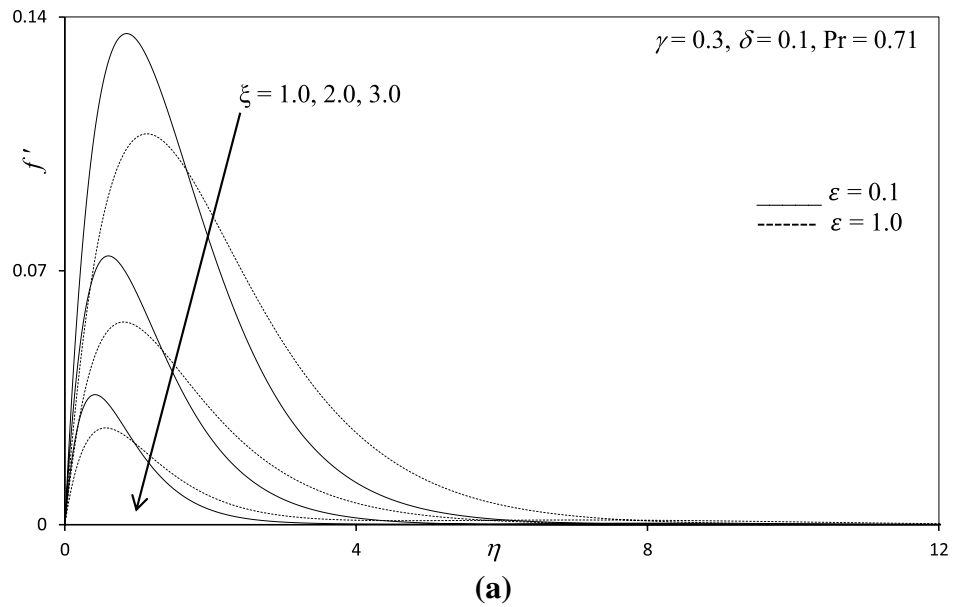


unlike the vast majority of other dimensionless thermo-fluid numbers. Higher Pr values imply a thinner thermal boundary layer thickness and more uniform temperature distributions across the boundary layer. Hence the thermal boundary layer will be much reduced in thickness compared with the hydrodynamic (momentum) boundary layer. $Pr < 1$ corresponds to greater thermal diffusion rate compared with momentum diffusion rate. A lower Pr ($Pr = 0.71$, i.e. gas) implies that the fluid possess higher thermal conductivity (and an associated thicker thermal boundary layer structure) so that heat can diffuse away from the fluid to the plate surface faster than for higher Pr

fluid ($Pr = 7.0$, i.e. liquids associated with thinner boundary layers).

Figure 7a, b depicts the velocity (f') and temperature (θ) distributions with radial coordinate, for various transverse (stream wise) coordinate values, ξ along with the variation in the fluid parameter ε . Clearly, from these figures it can be seen that as suction parameter ξ increases, the maximum fluid velocity decreases. This is due to the fact that the effect of the suction is to take away the warm fluid on the vertical plate and thereby decrease the maximum velocity with a decrease in the intensity of the natural convection rate. Figure 7b shows the effect of the local suction

Fig. 7 **a** Influence of ξ on velocity profiles, **b** influence of ξ on temperature profiles



parameter on the temperature profiles. It is noticed that the temperature profiles decrease with an increase in the suction parameter and as the suction is increased, more warm fluid is taken away and this the thermal boundary layer thickness decreases. It is also seen that with an increase in ϵ , the impedance offered by the fibers of the porous medium will increase and this will effectively decelerate the flow in the regime, as testified to by the evident decrease in velocities shown in Fig. 7a.

Figure 8a, b depicts the velocity (f') and temperature (θ) distributions with radial coordinate, for various transverse (stream wise) coordinate values, ξ , along with the variation in the fluid parameter δ . Clearly, from these figures it

can be seen that as suction parameter ξ increases, the maximum fluid velocity decreases. This is due to the fact that the effect of the suction is to take away the warm fluid on the vertical plate and thereby decrease the maximum velocity with a decrease in the intensity of the natural convection rate. Figure 8b shows the effect of the local suction parameter on the temperature profiles. It is noticed that the temperature profiles decrease with an increase in the suction parameter and as the suction is increased, more warm fluid is taken away and this the thermal boundary layer thickness decreases.

Figure 9a, b depicts the influence of the Biot number, γ , on the dimensionless skin friction coefficient and heat

Fig. 8 **a** Influence of ξ and on velocity profiles, **b** influence of ξ and on temperature profiles

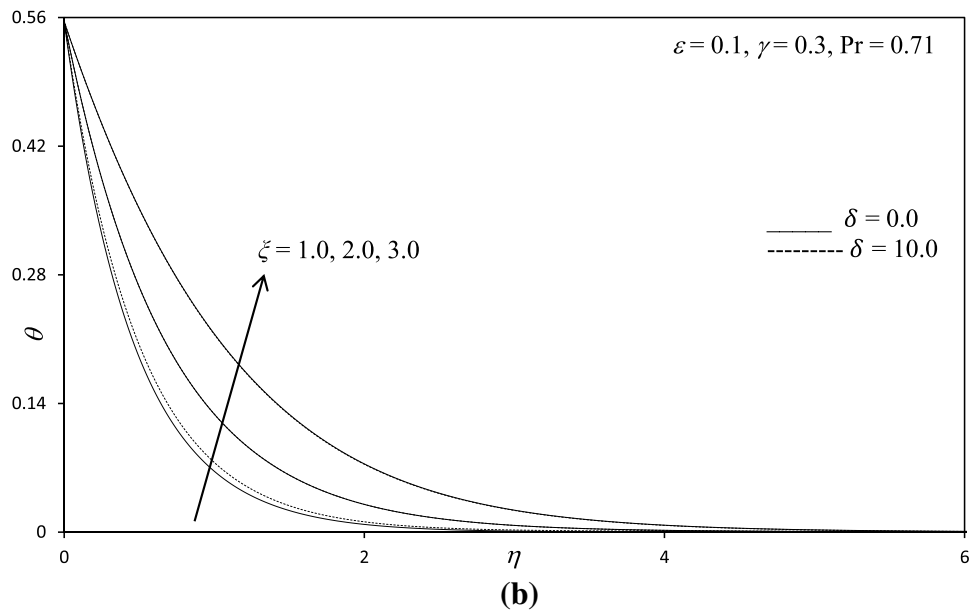
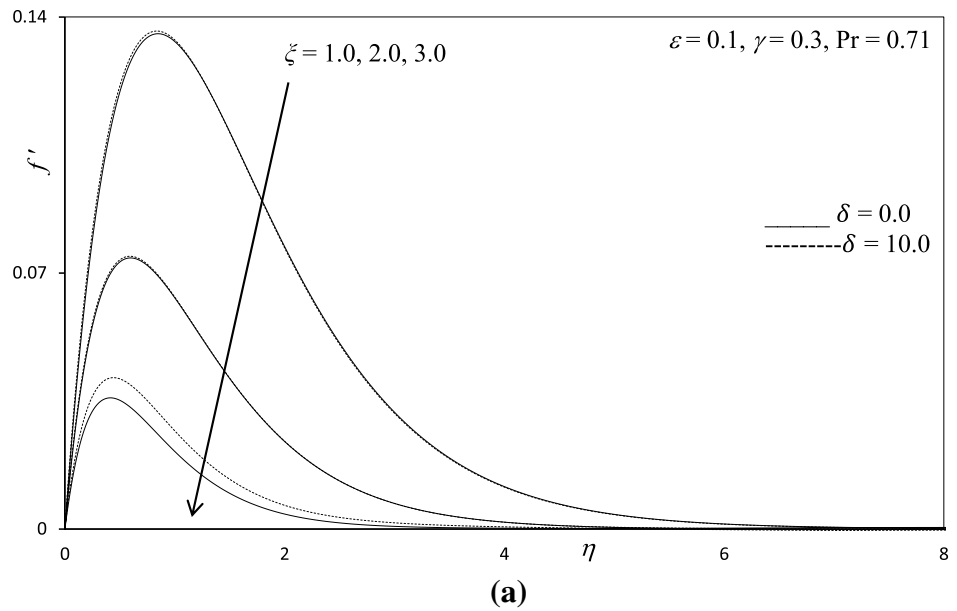


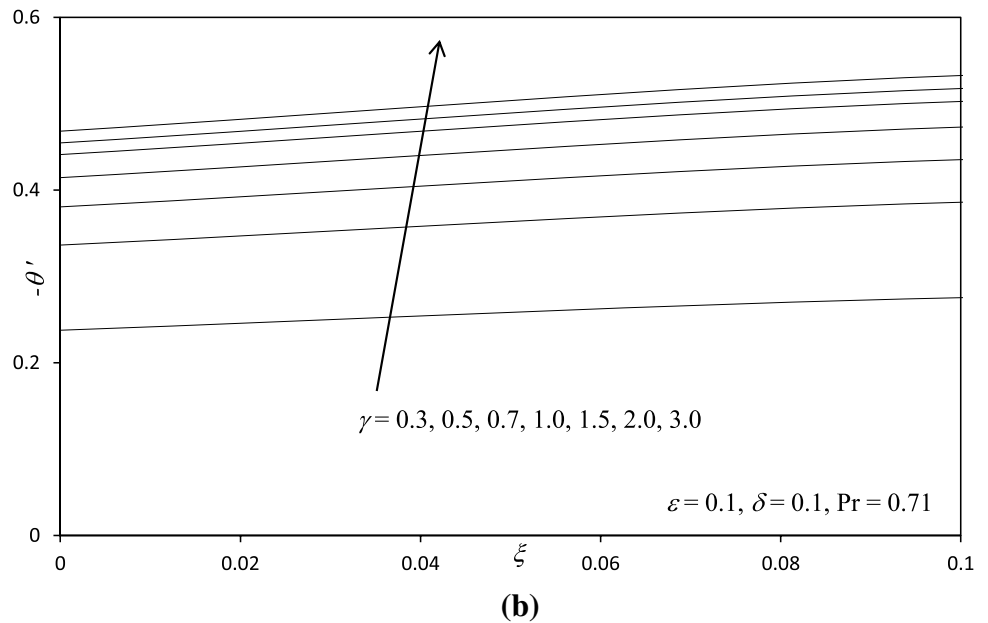
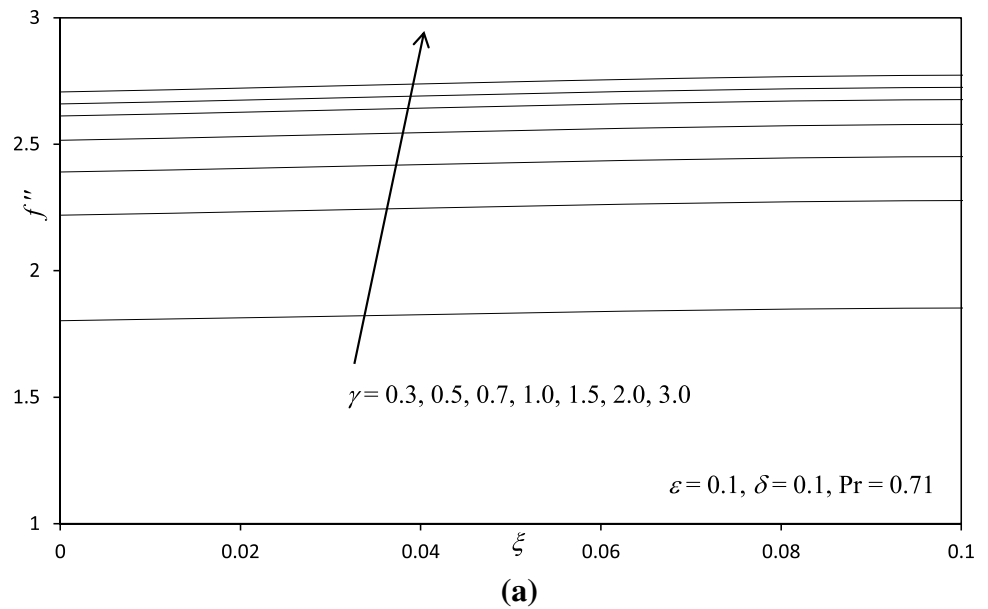
Table 6 Comparison values of $f''(\xi, 0)$ and $-\theta'(\xi, 0)$ for different values of ξ with $\varepsilon = \delta = 0.0$, $\gamma = 0.3$, $Pr = 1.0$

| ξ | Hossain et al. [41] | | Present | |
|-------|---------------------|--------------------|---------------|--------------------|
| | $f''(\xi, 0)$ | $-\theta'(\xi, 0)$ | $f''(\xi, 0)$ | $-\theta'(\xi, 0)$ |
| 0.1 | 0.0655 | 6.4627 | 0.0653 | 6.4626 |
| 0.2 | 0.1316 | 3.4928 | 0.1313 | 3.4924 |
| 0.4 | 0.2647 | 2.0229 | 0.2644 | 2.0225 |
| 0.6 | 0.3963 | 1.5439 | 0.3960 | 1.5436 |
| 0.8 | 0.5235 | 1.3247 | 0.5232 | 1.3243 |
| 1.0 | 0.6429 | 1.1995 | 0.6427 | 1.1992 |
| 1.5 | 0.8874 | 1.0574 | 0.8872 | 1.0571 |

transfer rate at the plate surface. The skin friction at the plate surface is seen to enhance greatly with rising γ values. This is principally attributable to the decrease in Grashof (free convection) number which results in an acceleration in the boundary layer flow, as elaborated by Chen and Chen [51]. Heat transfer rate (local Nusselt number) is also enhanced with increasing γ , as computed in Fig. 9b.

Figure 10a, b presents the influence of Eyring–Powell fluid parameter, ε , on dimensionless skin friction coefficient and heat transfer rate at the plate surface. It is observed that the dimensionless skin friction is elevated with the increase in ε , i.e. the boundary layer flow is accelerated with decreasing viscosity effects in the non-Newtonian regime.

Fig. 9 **a** Influence of γ on velocity profiles, **b** influence of γ on temperature profiles



Conversely, the surface heat transfer rate is substantially *decreased* with increasing ε values. Decreasing viscosity of the fluid (induced by increasing the ε value) reduces thermal diffusion as compared with momentum diffusion. A decrease in heat transfer rate at the wall implies less heat is convected from the fluid regime to the plate, thereby heating the boundary layer and enhancing temperatures.

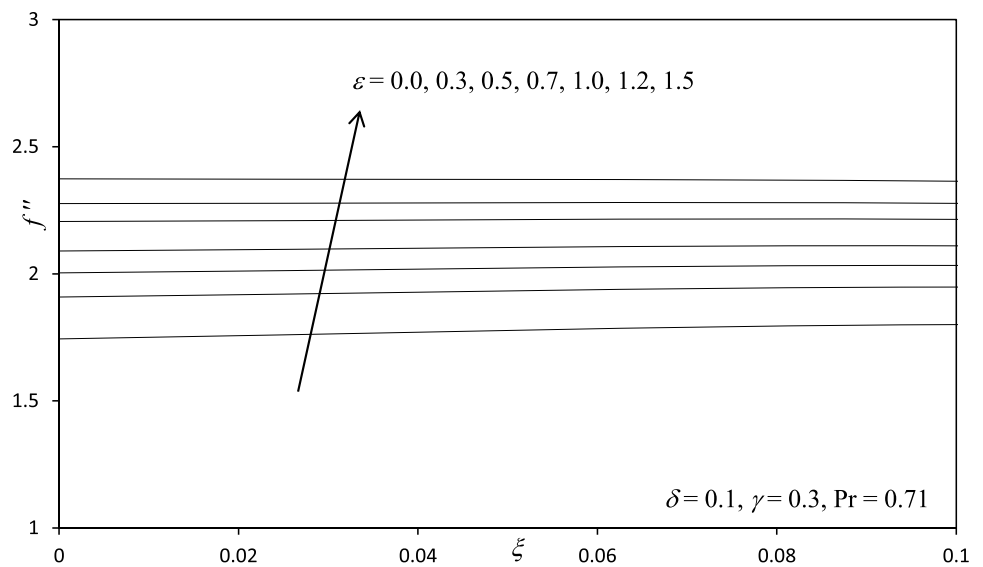
Figure 11a, b illustrates the influence of the local non-Newtonian parameter, δ , on the dimensionless skin friction coefficient and heat transfer rate. The skin friction (Fig. 11a) at the plate surface is reduced with increasing δ , however, only for very large values of the transverse

coordinate, ξ . The flow is, therefore, strongly accelerated along the curved plate surface far from the lower stagnation point. Heat transfer rate (local Nusselt number) is increased with increasing δ , *again at large values of ξ* , as computed in Fig. 11b.

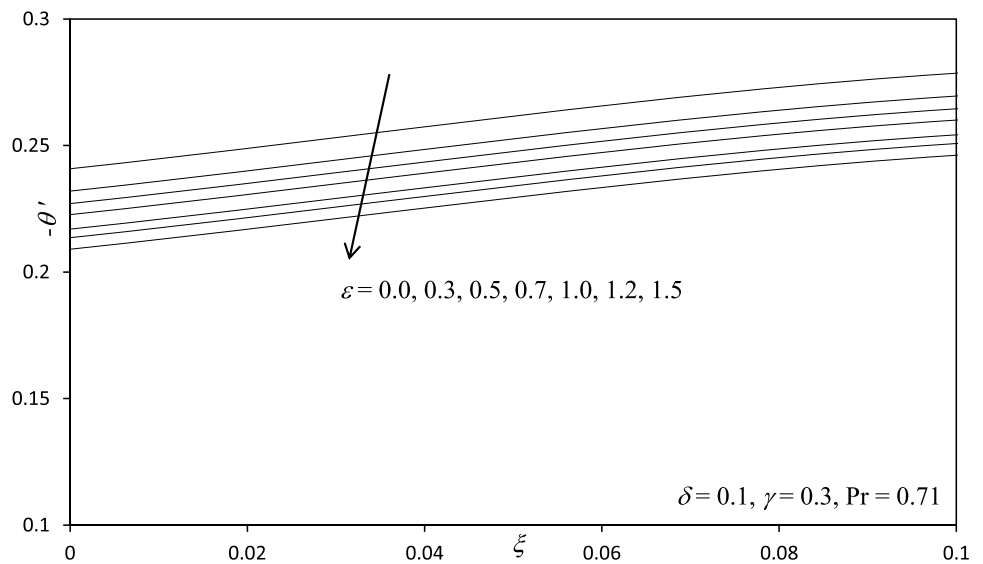
6 Conclusions

Numerical solutions have been presented for the boundary-driven flow and heat transfer of non-Newtonian Eyring–Powell fluid from a vertical porous plate. The

Fig. 10 **a** Influence of ε on velocity profiles, **b** influence of ε on temperature profiles



(a)

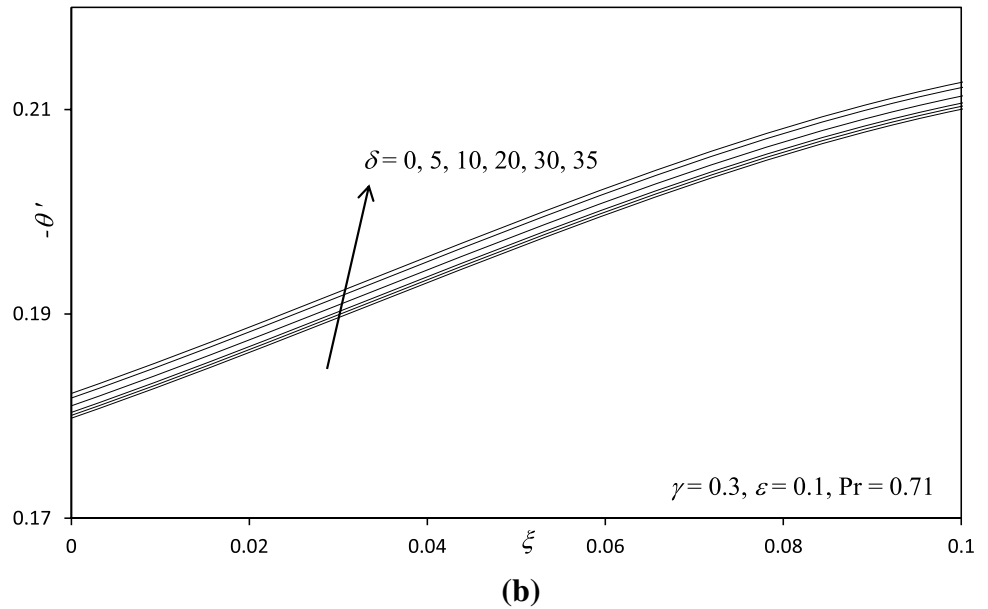
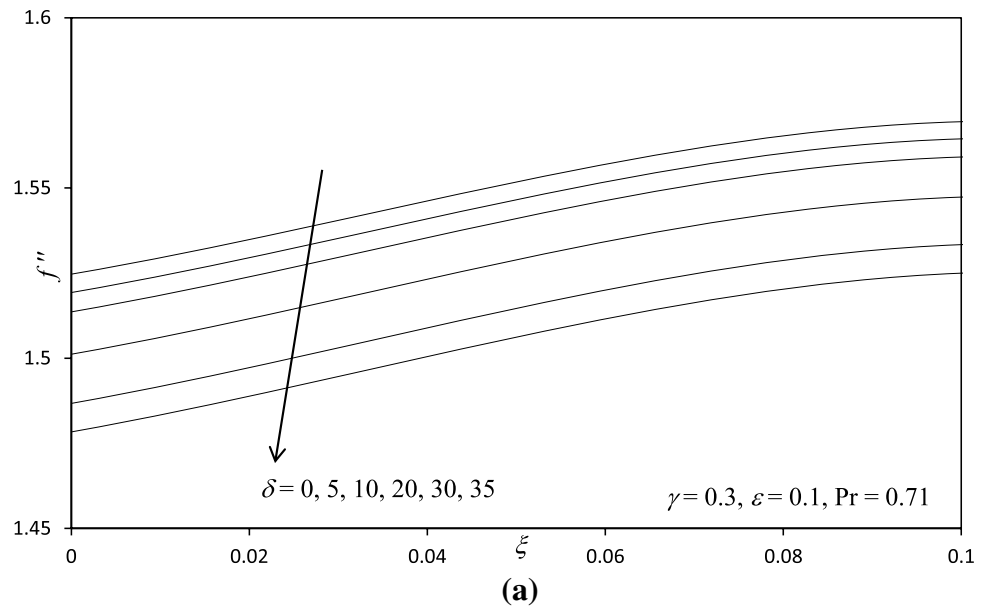


(b)

Keller-box implicit second-order accurate finite difference numerical scheme has been utilized to efficiently solve the transformed, dimensionless velocity and thermal boundary layer equations, subject to realistic boundary conditions. A comprehensive assessment of the effects of Eyring–Powell fluid parameter (ε), local non-Newtonian parameter (δ), Biot number (γ), Prandtl number (Pr) and dimensionless tangential coordinate (ξ) on thermo-fluid characteristics has been conducted. Excellent correlation with previous studies has been demonstrated testifying to the validity of the present code. Generally, very stable and accurate solutions are obtained

with the present finite difference code. The numerical code is able to solve nonlinear boundary layer equations very efficiently and, therefore, shows excellent promise in simulating transport phenomena in other non-Newtonian fluids. It is, therefore, presently being employed to study micropolar fluids and viscoplastic fluids which also simulate accurately many chemical engineering working fluids in *curved* geometrical systems. The present study has also neglected time effects. Future simulations will also address *transient* polymeric boundary layer flows and will be presented soon.

Fig. 11 **a** Influence of δ on velocity profiles, **b** influence of δ on temperature profiles



References

1. Qing J, MubashirBhatti M, Abbas MA, Rashidi MM, El-Sayed Ali M (2016) Entropy generation on MHD Casson Nanofluid flow over a porous stretching/shrinking surface. *Entropy* 18(4). doi:10.3390/e18040123
2. Norouzi M, Davoodi M, Anwar Bég O, Joneidi AA (2013) Analysis of the effect of normal stress differences on heat transfer in creeping viscoelastic Dean flow. *Int J Therm Sci* 69:61–69
3. Rashidi MM, Keimanesh M, Anwar Bég O, Hung TK (2011) Magneto-hydrodynamic biorheological transport phenomena in a porous medium: a simulation of magnetic blood flow control. *Int J Numer Methods Biomed Eng* 27(6):805–821
4. Mustafa M, Khan JA, Hayat T, Alsaedi A (2015) Simulations for Maxwell fluid flow past a convectively heated exponentially stretching sheet with nanoparticles. *AIP Advances* 5(3):037133
5. MubashirBhatti Muhammad, Abbas Tehseen, Rashidi MM, El-Sayed Ali M (2016) Numerical simulation of entropy generation with thermal radiation on MHD carreau nanofluid towards a shrinking sheet. *Entropy* 18(6):200. doi:10.3390/e18060200
6. Bhatti MM, Abbas T, Rashidi MM (2016) Numerical study of entropy generation with nonlinear thermal radiation on magneto-hydrodynamics non-newtonian nanofluid through a porous shrinking sheet. *J Magn* 21(3):468–475
7. Bhatti MM, Rashidi MM (2016) Effect of thermos-diffusion and thermal radiation on Williamson Nanofluid over a porous shrinking/stretching sheet. *J Mol Liq* 221:567–573

8. Abdul gaffar S, Ramachandra Prasad V, Keshava Reddy E (2016) Computational study of Jeffrey's non-Newtonian fluid past a semi-infinite vertical plate with thermal radiation and heat generation/absorption. *Ain Shams Eng J*. doi:[10.1016/j.asej.2016.09.003](https://doi.org/10.1016/j.asej.2016.09.003)
9. Ishak A (2010) Similarity solutions for flow and heat transfer over a permeable surface with convective boundary condition. *Appl Math Comput* 217(2):837–842
10. Aziz A (2009) A similarity solution for laminar thermal boundary layer over a flat plate with a convective surface boundary condition. *Commun Nonlinear Sci Numer Simul* 14(4):1064–1068
11. Aziz A (2010) Hydrodynamic and thermal slip flow boundary layers over a flat plate with constant heat flux boundary condition. *Commun Nonlinear Sci Numer Simul* 15(3):573–580
12. Makinde OD, Olanrewaju PO (2010) Buoyancy effects on thermal boundary layer over a vertical plate with a convective surface boundary condition. *Trans ASME J Fluids Eng* 132(4):044502
13. Makinde OD, Aziz A (2010) MHD mixed convection from a vertical plate embedded in a porous medium with a convective boundary condition. *Int J Therm Sci* 49(9):1813–1820
14. Gupta D, Kumar L, Anwar Bég O, Singh B (2014) Finite element simulation of mixed convection flow of micropolar fluid over a shrinking sheet with thermal radiation. *Proc I Mech E Part E J Process Mech Eng* 228(1). doi:[10.1177/0954408912474586](https://doi.org/10.1177/0954408912474586)
15. Swapna G, Kumar L, Anwar Bég O, Singh B (2015) Finite element analysis of radiative mixed convection magneto-micropolar flow in a Darcian porous medium with variable viscosity and convective surface condition. *Heat Transf Asian Res* 44(6):515–532
16. Makinde OD, Zimba K, Anwar Bég O (2012) Numerical study of chemically-reacting hydromagnetic boundary layer flow with Soret/Dufour effects and a convective surface boundary condition. *Int J Therm Environ Eng* 4(1):89–98
17. Anwar Bég O, Uddin MJ, Rashidi MM, Kavyani N (2014) Double-diffusive radiative magnetic mixed convective slip flow with Biot number and Richardson number effects. *J. Engineering Thermophysics* 23(2):79–97
18. Subhashini SV, Samuel N, Pop I (2011) Double-diffusive convection from a permeable vertical surface under convective boundary condition. *Int Commun Heat Mass Transf* 38(9):1183–1188
19. Hayat T, Hussain Z, Alsaedi A, Mustafa M (2017) Nanofluid flow through a porous space with convective conditions and heterogeneous-homogeneous reactions. *J Taiwan Inst Chem Eng* 70:119–126
20. Ahmad R, Mustafa M (2016) Model and comparative study for rotating flow of nanofluids due to convectively heated exponentially stretching sheet. *J Mol Liq* 220:635–641
21. Khan JA, Mustafa M, Mushtaq A (2016) On three-dimensional flow of nanofluids past a convectively heated deformable surface: A numerical study. *Int J Mass Transf* 94:49–55
22. Khan JA, Mustafa M, Hayat T, Alsaedi A (2015) Numerical study on three-dimensional flow of nanofluid past a convectively heated exponentially stretching sheet. *Can J Phys* 93(10):1131–1137
23. Powell RE, Eyring H (1944) Mechanism for relaxation theory of viscosity. *Nature* 154:427–428
24. Hayat T, Zubair M, Waqas M, Alsaedi A, Ayub M (2017) On doubly stratified chemically reactive flow of Powell-Eyring liquid subject to non-Fourier heat flux theory. *Res Phys* 7:99–106
25. Khan NA, Sultan F, Rubbab Q (2015) Optimal solution of non-linear heat and mass transfer in a two-layer flow with nano-Eyring–Powell fluid. *Res Phys* 5:199–205
26. Hayat T, Ullah I, Alsaedi A, Farooq M (2017) MHD flow of Powell-Eyring nanofluid over a non-linear stretching sheet. *Res Phys* 7:189–196
27. Khalil-Ur-Rehman, Malik MY, Makinde OD (2017) Parabolic curve fitting study of subject to joule heating in MHD thermally stratified mixed convection stagnation point flow of Eyring–Powell fluid induced by an inclined cylindrical surface. *J King Saud Univ Sci*. doi:<http://dx.doi.org/10.1016/j.jksus.2017.02.003>
28. Waqas M, Ijaz Khan M, Hayat T, Alsaedi A, Imran Khan M (2017) On Cattaneo-Christov heat flux impact for temperature-dependent conductivity of Powell-Eyring liquid. *Chin J Phys*. doi:[10.1016/j.cjph.2017.02.003](https://doi.org/10.1016/j.cjph.2017.02.003)
29. Hina S, Mustafa M, Hayat T, Alsaedi A (2016) Peristaltic transport of Powell-Eyring fluid in a curved channel with heat/mass transfer and wall properties. *Int J Heat Mass Transf* 101:156–165
30. Hayat T, NaseemAslam M Rafiq, Alsaedi Fuad E (2017) Hall and Joule heating effects on peristaltic flow of Powell-Eyring in an inclined symmetric channel. *Res Phys*. doi:[10.1016/j.rinp.2017.01.008](https://doi.org/10.1016/j.rinp.2017.01.008)
31. Hayat T, Sajjad R, Muhammed T, Alsaedi A, Ellahi R (2017) On MHD nonlinear stretching flow of Powell-Eyring nanomaterial. *Res Phys*. doi:<http://dx.doi.org/10.1016/j.rinp.2016.12.039>
32. Bhatti MM, Abbas T, Rashidi MM, El-Sayed Ali M, Yang Z (2016) Entropy generation on MHD Eyring–Powell nanofluid through a permeable stretching surface. *Entropy* 18(6). doi:[10.3390/e18060224](https://doi.org/10.3390/e18060224)
33. Abdul Gaffar S, Ramachandra Prasad V, Keshava Reddy E (2016) Non-Newtonian thermal convection from an isothermal sphere with Biot number effects. *Int J Ind Math* 8(2)
34. Abdul Gaffar S, Ramachandra Prasad V, Keshava Reddy E, Anwar Beg O (2014) Computational study of non-Newtonian thermal convection from a vertical porous plate in a non-Darcy porous medium with Biot number effects. *J Porous Media* 17(7):601–622
35. S Abdul Gaffar, V Ramachandra Prasad, B Vijaya, O Anwar Beg (2015) Mixed convection flow of magnetic viscoelastic polymer from a non-isothermal wedge with Biot number effects. *Int J Eng Maths* 2015:15 (Article ID 287623)
36. Abdul Gaffar S, Ramachandra Prasad V, Keshava Reddy E (2016) MHD free convection flow of non-Newtonian Eyring–Powell fluid from vertical surface in porous media with Hall/Ion-slip currents and Ohmic dissipation. *Alex Eng J* 55:875–905
37. Patel M, Timol MG (1986) Similarity solutions of boundary layer flow of non-Newtonian fluids. *Int J Nonlinear Mech* 21(6):475–481
38. Keller HB (1978) Numerical methods in boundary-layer theory. *Ann Rev Fluid Mech* 10:417–433
39. Anwar Bég O (2012) Numerical methods for multi-physical magnetohydrodynamics, Chapter 1. *New Developments in Hydrodynamics Research*, Nova Science, New York, September, 2012, pp 1–112
40. Ramachandra Prasad V, Abdul Gaffar S, Anwar Beg O (2015) Non-similar computational solutions for free convection boundary-layer flow of a Nanofluid from an isothermal sphere in a non-Darcy porous medium. *J Nanofluids* 4(2):1–11
41. Ramachandra Prasad V, Abdul Gaffar S, Anwar Beg O (2015) Heat and mass transfer of a Nanofluid from a Horizontal cylinder to a Micropolar fluid. *AIAA J Thermophys Heat Transf* 29(1):127–139
42. Javed M, Hayat T, Mustafa M, Ahmad B (2016) Velocity and thermal slip effects on peristaltic motion of Walters-B fluid. *Int J Heat Mass Transf* 96:210–217
43. Abdul Gaffar S, Ramachandra Prasad V, Keshava Reddy E, Anwar Beg O (2017) Magnetohydrodynamic free convection boundary layer flow of non-Newtonian tangent hyperbolic fluid from a vertical permeable cone with variable surface temperature. *J Braz Soc Mech Sci Eng* 39(1):101–116
44. Abdul Gaffar S, Ramachandra Prasad V, Keshava Reddy E (2016) Magnetohydrodynamics flow of Non-Newtonian fluid

- from a vertical permeable cone in the presence of thermal radiation and heat generation/absorption. *Int J Appl Comput Math*. doi:[10.1007/s40819-016-0262-8](https://doi.org/10.1007/s40819-016-0262-8)
45. Bilal S, Ur Rehman K, Malik MY (2017) Numerical investigation of thermally stratified Williamson fluids flow over a cylindrical surface via Keller box method. *Res Phys*. doi:[10.1016/j.rinp.2017.01.032](https://doi.org/10.1016/j.rinp.2017.01.032)
 46. Prasad VR, Vasu B, Anwar Bég O, Parshad DR (2012) Thermal radiation effects on magnetohydrodynamic free convection heat and mass transfer from a sphere in a variable porosity regime. *Commun Nonlinear Sci Numer Simul* 17(2):654–671
 47. Hossain MA, Alim MA, Rees DAS (1999) The effect of radiation on free convection flow from a porous vertical plate. *Int J Heat Mass Transf* 42:181–191
 48. Rohsenow WM, Hartnett JP, Ganic EN (1985) *Handbook of heat transfer fundamentals*, 2nd edn. Mac-Graw-Hill, New York
 49. Incropera D, DeWitt D (1981) *Fundamentals of heat and mass transfer*. Wiley, New York
 50. Schlichting H (2000) *Boundary-layer theory*, 8th edn. Mac-Graw-Hill, New York
 51. Chen H-T, Chen C-K (1988) Natural convection of a non-Newtonian fluid about a horizontal cylinder and a sphere in a porous medium. *Int Commun Heat Mass Transf* 15(5):605–614. doi:[10.1016/0735-1933\(88\)90051-6](https://doi.org/10.1016/0735-1933(88)90051-6)